aerospace

MDPI

Article

Anisotropic Turbulent Kinetic Energy Budgets in Compressible Rectangular Jets

Kalyani Bhide * and Shaaban Abdallah

Department of Aerospace Engineering and Engineering Mechanics, University of Cincinnati, Cincinnati, OH 45221, USA
* Correspondence: bhidekr@mail.uc.edu

Abstract: Turbulence is governed by various mechanisms, such as production, dissipation, diffusion, dilatation and convection, which lead to its evolution and decay. In high-speed flows, turbulence becomes complicated due to compressibility effects. Therefore, the goal of the current work is to characterize these mechanisms in rectangular supersonic jets by directly evaluating their contributions in turbulent kinetic energy (TKE) budget equation. The budgets are obtained using high-fidelity Large Eddy Simulations that employ WALE subgrid-scale model. Jet nearfield data are validated with PIV experimental measurements, available from the literature, which include mean flow and second-order statistics. To ensure spatial resolution and temporal convergence of higher-order statistics, qualitative performance metrics are presented. The results indicate that TKE production is the major source term, while pressure-dilatation term acts as a sink throughout the development of the jet. The diffusion term has the highest contribution from triple-velocity correlations, followed by pressure diffusion and molecular diffusion. Subgrid-scale diffusion and dissipation are also evaluated and their contributions are minimal. Each term is presented on both minor and major axis plane and reveals asymmetry in the statistics. A detailed explanation of budget contributions is provided, leading to the mechanisms responsible for the anisotropy of TKE.

Keywords: turbulent kinetic energy budget; supersonic jet; anisotropy; turbulence; shear layer

Citation: Bhide, K.; Abdallah, S. Anisotropic Turbulent Kinetic Energy Budgets in Compressible Rectangular Jets. *Aerospace* **2022**, *9*, 484. https://doi.org/10.3390/aerospace9090484

Academic Editors: Konstantinos Kontis

Received: 18 July 2022
Accepted: 24 August 2022
Published: 30 August 2022

1. Introduction

Turbulence is a complicated non-linear phenomenon, which is governed by various large-scale and small-scale transfer mechanisms. Numerical simulation of turbulent flows is a vast field that is primarily based on resolving the length and time scales as well as capturing the unresolved scales [1]. Understanding of turbulent flows can be improved by analyzing energy budgets since they help quantify various underlying transport mechanisms by directly examining their contributions. TKE budget equation not only provides the main mechanisms responsible for turbulence evolution and decay but also provides direction towards improving the current turbulence models [1]. The terms in TKE budget equation are known as the budget terms and they help in quantifying the local turbulence gain and loss mechanisms. Calculation of energy budget terms relies upon both second- and higher-order fluctuating terms as well as mean flow gradients. Therefore, gaining access to higher-order fluctuating terms is crucial to obtain energy budgets. In RANS, these terms are modeled by correlating them with mean flow gradients and so higher-order statistics cannot be directly accessed. In LES, since large scales of the flow are resolved, gaining access to higher-order statistics becomes possible. Although DNS solves the governing equations directly without the use of modeling, it is very expensive for high Reynolds number flows. Therefore, LES is the appropriate choice for budget analysis of high Reynolds number flows considering the costs associated with DNS. High-speed flows occur in aerospace application and are fundamentally crucial to understand due to the complex flow behavior involving shock–boundary layer or shock–shear layer interactions. In

such flows, density and pressure fluctuations are typically significant and are characterized by a set of shock waves and expansion fans. These features affect the turbulent mixing process. While such flows have been studied previously, limited literature is available that directly computes the budget terms in these flows because gaining access to all terms in the TKE equation is quite challenging/expensive, both experimentally and numerically, due to numerous reasons. One of the reasons is the presence of higher-order statistics—mainly the pressure velocity correlations and their measurements in experiments. Another challenge is ensuring relevant scales are resolved. As a result, the numerical simulations need to be conducted for a sufficiently long time for convergence of budget terms. Therefore, the goal of this paper is to examine the turbulence transport mechanisms in supersonic jets by means of LES with WALE subgrid-scale model to gain insights into the evolution of the jet from a TKE budget standpoint.

Before diving deeper into the goals of the current paper, we take a closer look at the literature review to highlight the importance of budget analysis. Section 1.1 details a brief overview of budget analysis from literature for turbulent flows occurring in various applications—both incompressible and compressible regimes. Section 1.2 details the TKE budget equation used in this work and explains various terms associated with it. Section 1.3 provides a brief overview of LES solvers in the literature because the numerical modeling approach directly affects the resultant budget quantities and so the choice of solver is an important topic.

1.1. Budget Analysis of Incompressible and Compressible Flow in Open Literature

This subsection presents an overview of budget analysis, both experimentally and numerically. It also briefly describes which terms were directly computed and how and which terms were obtained as a balance. A well-known study on planar jets dates back to the 1970s. Gutmark et al. [2] conducted an experimental investigation of a planar incompressible jet using hot-wire anemometry to directly measure the mean velocities as well as third- and fourth-order terms. Nishino et al. [3] conducted measurements on impinging axisymmetric water jet at Reynolds number ~13,000 in the stagnation region using two- and three-dimensional particle-tracking velocimetry. More recently, experimental investigation on a rectangular incompressible jet was published by Cavo et al. [4]. They measured the TKE and enstrophy budgets using their in-house hot wire and computed spatial derivatives of fluctuating velocities in all three directions. While they obtained production, advection and dissipation by measurements, diffusion was obtained by subtraction. Liu et al. [5] conducted experimental measurements of TKE budget in planar wake flow. While they measured convection, turbulence diffusion and turbulence production, the pressure diffusion term was obtained by forcing a balance of TKE transport equation and dissipation was estimated using a locally axisymmetric turbulence assumption. These studies were based on experimental investigation. Others also presented the TKE budgets based on numerical investigation. Bogey and Bailly [6,7] derived TKE budget and Reynolds stress transport equation in their paper on a round compressible jet and conducted LES to compute the contribution of each term. They also presented the filtering dissipation due to LES filter. Another recent study was published by Bonelli et al. [8]. They conducted LES using an in-house solver to directly compute each term in the TKE transport equation for a round compressible jet at Mach number 1.4 and 2.6 and with Reynolds numbers ranging from 2500 to 20,000. Their analysis presented the budgets on only one plane of symmetry, i.e., the XY plane, since it was a round jet. Vyas et al. [9] demonstrated the TKE budgets in shock-wave boundary layer interactions using implicit LES focusing on wall-bounded flow. While their research provided the statistics during SBLI, they pointed that their LES grid size was inadequate in the close vicinity of the wall. Kokkinakis et al. [10] evaluated the TKE budgets in a compression ramp using DNS to reveal their contributions during SBLI.

While these studies revealed the budgets for compressible flow, others have shown TKE budgets for different applications. Orlandi et al. [11] conducted DNS of a circular pipe flow with smooth and rough walls to obtain the TKE budgets. Tian et al. [12] conducted bud-

get analysis of flow over urban-like canopy using LES with dynamic Smagorinsky model. Watanabe et al. [13] conducted implicit LES for low Reynolds number turbulent planar jet to analyze the budget terms, except for the dissipation term, which was obtained as a balance. Lai et al. [14] presented the budgets for a low Reynolds number water jet using stereoscopic particle image velocimetry (SPIV) and compared the results with experimental data from an air jet. Zhang et al. [15] estimated the TKE budgets in a high wind boundary layer of a hurricane and indicated that shear production and dissipation are the major source and sink terms. Wu et al. [16] demonstrated the budgets in wind turbine wakes using LES. Zippel et al. [17] presented the budgets for ocean surface mixed layer. Balakumar et al. [18] demonstrated the budgets using DNS and RANS for turbulent flows through a plane channel and a channel with a constriction. Apart from high-fidelity approaches, RANS-based investigations have also been conducted to examine the budget terms, mainly production and dissipation. For example, Siddappaji et al. [19,20] demonstrated the dissipation of kinetic energy in unducted rotors. Vorticity-dynamics-based assessment of loss propagation in turbomachinery flows using Spalart–Allmaras turbulence model was also discussed [21,22]. Gao [23] demonstrated budgets for compressor cascade using a two-equation turbulence model. Monier et al. [24] demonstrated the budgets for tip-leakage flow using RANS and LES. Chen et. al [25] demonstrated flow diagnostics of a transonic compressor rotor using boundary vorticity flux to capture on-wall signatures of vorticity and skin-friction vector line at RANS level. Boundary vorticity flux is another method of capturing flow turbulence characteristics. These works were primarily based on RANS modeling.

Overall, budget analysis is general and fundamentally helpful to enhance the understanding of turbulent flows occurring in various applications. While previous studies shed some light on budget analysis for incompressible low-speed flows as well as high-speed axisymmetric jets, such analysis has not yet been shown for rectangular jets at supersonic speeds. Therefore, this paper aims to bridge the gap. In our previous work, non-linear eddy viscosity and Reynolds stress model-based investigation was conducted to capture the anisotropy of turbulence [26,27]. TKE production term was evaluated using WALE subgrid-scale LES and non-linear eddy viscosity-based two-equation RANS model. However, a complete account of each term in the budget equation was not presented. As a continuation of prior work, this paper presents the budget analysis for each term in the TKE transport equation. Since rectangular jets are non-axisymmetric jets, the anisotropy of TKE exists on the minor and major axis plane. Through this work, the mechanisms responsible for the asymmetry of TKE from a budget standpoint are presented. This approach directly captures the TKE at fundamental governing equation level, thus, providing insights into the underlying turbulence mechanisms.

1.2. TKE Budget Equation

In the context of budget analysis, it is paramount to take a closer look at the budget equation itself. The terms associated with budget equation can change in the context of incompressible vs. compressible flow so, many forms have been presented in the literature. The one used in the present work is from Wilcox [1]. TKE budget equation is typically derived by multiplying the momentum equation by a fluctuating velocity component and then performing Favre averaging or Reynolds averaging. In compressible flow, density fluctuations arise and the role of density averaging is to filter out the effect of density fluctuations on averaged quantities. According to Morkovin's hypothesis [28], turbulence is affected by compressibility when density fluctuations are significant, while Bradshaw [29] highlighted that this effect may be reflected in compressible shear layers at low Mach numbers ~1.5. Following this, density averaging is considered in the current work. Equation (1) is the Favre-averaged TKE transport equation. It contains two additional terms—pressure dilatation and pressure work—as compared to its incompressible counterpart. The first term on RHS is mean flow convection, the second term is production from mean flow gradients and Reynolds stresses, the third term is viscous dissipation, the fourth term is subgrid-scale dissipation, the fifth term is molecular diffusion and the

sixth term is subgrid-scale diffusion. The seventh term is turbulence diffusion and the eighth is pressure diffusion. The ninth term is pressure work and the second-last term is pressure dilatation. Here, an overbar denotes time/ensemble-averaged quantity, ˜ denotes Favre-averaged quantity and $''$ denotes fluctuation in Favre-averaged quantity. TKE is defined as $k = \frac{1}{2}\overline{u_i'' u_i''}$. The resolved TKE transport equation contains two additional terms due to the subgrid-scale stress and they are subgrid-scale diffusion and subgrid-scale dissipation. These two terms are also calculated from LES. Finally, to balance the budget, a residual denoted as R is calculated. The residual is a numerical phenomenon rather than physical. In the below equation, ρ is the density, p is the pressure, u is the streamwise component of velocity, τ_{ij} is the Reynolds stress tensor, t_{ji} is the resolved part of viscous stress tensor and t_{SGS} is the subgrid-scale stress tensor obtained using WALE subgrid-scale model. P is the mean pressure. Further explanations on the computation of budgets are provided in the Methodology section.

$$0 = \underbrace{-\frac{\partial}{\partial x_j}\left(\overline{\rho}\widetilde{u}_j k\right)}_{C} + \underbrace{\overline{\rho}\tau_{ij}\frac{\partial \widetilde{u}_i}{\partial x_j}}_{T_P} \underbrace{-\overline{t_{ji}\frac{\partial u_i''}{\partial x_j}}}_{V_{Ds}} \underbrace{-\overline{t_{SGS}\frac{\partial u_i''}{\partial x_j}}}_{SGS_{Ds}} + \underbrace{\frac{\partial}{\partial x_j}\left(\overline{t_{ji}u_i''}\right)}_{M_{Df}} + \underbrace{\frac{\partial}{\partial x_j}\left(\overline{t_{SGS}u_i''}\right)}_{SGS_{Df}} \underbrace{-\frac{\partial}{\partial x_j}\left(\overline{\rho u_i'' \frac{1}{2} u_i'' u_i''}\right)}_{T_{Df}} \underbrace{-\frac{\partial}{\partial x_j}\left(\overline{p' u_j''}\right)}_{P_{Df}} \underbrace{-\overline{u_i''}\frac{\partial P}{\partial x_i}}_{P_W} + \underbrace{\overline{p'\frac{\partial u_i''}{\partial x_i}}}_{P_D} + R \quad (1)$$

1.3. LES Solvers—Subgrid-Scale Turbulence and Applications

From Section 1.1, it is evident that LES is primarily used for budget investigations. Since numerical computation of budget terms is a direct measure of solver capabilities, this subsection highlights various LES solvers in the literature. Many LES solvers have been developed up until now, which are both in-house/non-commercial as well as commercial solvers. From the LES standpoint, it is crucial to model the subgrid-scale turbulence accurately. Therefore, it is important to understand how subgrid-scale turbulence is handled in each solver, as it directly affects the budget analysis. Discretization schemes are also important. The list in Table 1 may not be exhaustive, but the goal is to present the majority of the LES solvers. Note that the details listed in the table reflect the data reported in the literature and may not include exhaustive solver capabilities. Typically, when explicit subgrid-scale modeling is used, the subgrid-scale stresses are modeled using Boussinesq approximation. On the other hand, implicit LES relies on representing the subgrid-scale turbulence in terms of high-order dissipation schemes since turbulence is dissipative. Further, based on the LES approach, the filtering activity can also differ. Either way, the question of whether subgrid-scale turbulence is modeled as isotropic or anisotropic remains and it is believed that this subsection will provide an overview of the existing LES solver capabilities.

Table 1. LES solvers.

Name	Reference	Subgrid Turbulence	Application	Convective Flux Discretization	Filtering
ALESIA	Bogey et al. [30]	Explicit filtering	External	Thirteen-point stencil FD	Explicit
CharLES	Bres et al. [31]	Vreman	External	Second order accurate blend of central and upwind	Spatial
ECNSS	Karami et al. [32]	Modified Germano method	External	Sixth-order central FD	Spatial

Table 1. *Cont.*

Name	Reference	Subgrid Turbulence	Application	Convective Flux Discretization	Filtering
EDGE	Eliasson et al. [33]	Implicit LES	External	Second-order accurate node centered FV	-
FLEDS	Bonelli et al. [8]	Smagorinsky, Artificial-Fluid LES model	External	Sixth-order compact scheme, derived from Pade schemes	Spatial
GASFLOW-MPI	Zhang et al. [34]	Smagorinsky	External	Second-order accurate van Leer MUSCL	Cube-root of cell volume
HiFiLES	Lopez et al. [35]	WSM	Wall-bounded, external	ESFR high-order	Cube-root of cell volume
JENRE	Kailasnath et al. [36]	MILES	External	Flux-Corrected Transport	-
LAVA	Kiris et al. [37], Stich et al. [38]	Implicit, Vreman	Wall-bounded, external	Mid-point central differencing operator	-
Maple	Aprovitola et al. [39]	Smagorinsky	Incompressible	Third-order accurate FV upwind	Cube-root of cell volume
OpenFOAM	Weller [40]	Smagorisnky, one equation eddy viscosity	Wall-bounded, external	Second-order semi discrete non-staggered KNP	Cube-root of cell volume
WRLES	Debonis [41]	Implicit LES, Smagorinsky	External	Central difference	Solution filtering based on low-pass filter
Star-CCM+	*Present work*	*WALE*	*Wall-bounded, external*	*Second-order accurate bounded-central difference*	*Cube-root of cell volume*

2. Methodology

The methodology section details the nozzle geometry, computational domain and boundary conditions, followed by governing equations. It then briefly discusses the averaging of flow variables.

2.1. Nozzle Geometry

The nozzle geometry from minor axis plane of view is shown in Figure 1. It has a rectangular cross-section with aspect ratio (AR) = 2 with equivalent diameter = 20.65 mm and design Mach number = 1.5. The sharp throat causes a shock wave just downstream of the throat. This has been addressed in our previous work [42,43]. We explored the rectangular jet flowfield numerically focusing on both internal and external flow. Fluid-thermal-structural analysis for this nozzle was also conducted [44]. The nozzle is a small-scale prototype built for acoustic testing at University of Cincinnati's experimental facility. PIV based experimental investigation has been carried out by Baier et al. [45].

2.2. Governing Equations and Numerical Methods

The simulations in this work are conducted using a commercial finite volume solver Star-CCM+ version 15.04.008-R8 by Siemens [46]. The governing equations of mass, momentum and energy are listed below in the integral form since they are integrated over a finite control volume in the solver.

$$\frac{\partial}{\partial t}\int_V \rho dV + \oint_A \rho v.da = \int_V S_u dV \tag{2}$$

$$\frac{\partial}{\partial t}\int_V \rho v dV + \oint_A \rho v \otimes v.da = -\oint_A pI.da + \oint_A T.da + \int_V f_b dV + \int_V s_u dV \quad (3)$$

$$\frac{\partial}{\partial t}\int_V \rho E dV + \oint_A \rho H v.da = -\oint_A q.da + \oint_A T.vda + \int_V f_b.v dV + \int_V S_u dV \quad (4)$$

In above equations, ρ is the density, v is the velocity, p is the pressure, I is the identity tensor, T is viscous stress tensor, f_b is resultant of body forces, E is total energy and q is the heat flux. S_u is user-defined source term. H is total enthalpy. a is the area vector. V is the volume. Since the LES is based on WALE subgrid-scale model, the subgrid-scale stress tensor is approximated using Boussinesq hypothesis that relies on computing the eddy viscosity. The heat flux vector is given as $q = -\left(\kappa + \frac{\mu_t C_p}{Pr_t}\right)\nabla T$ where κ is thermal conductivity, C_p is specific heat, Pr_t is turbulent Prandtl number which is fixed at 0.9 and T is the temperature. Star-CCM+ uses an implicit filter as outlined in the user manual [46] and it is based on cube root of cell volume. Convective fluxes are discretized using bounded central difference scheme which is a blend of first-order accurate upwind as well as second-order accurate central difference scheme and second-order accurate upwind scheme. The scheme is weighted more towards the central differencing part. Among various schemes available in the solver, bounded central scheme offers both robustness and accuracy as compared to second-order upwind schemes [46]. Therefore, it is deemed appropriate here. Temporal discretization is based on first-order backward differencing formula. To account for the temperature-based variation in dynamic viscosity, Sutherland's law is used. To ensure the residuals of continuity, momentum and energy settled at the end of each time step, ten inner iterations were run for each time step and the values reached at least the order of 1×10^{-7}.

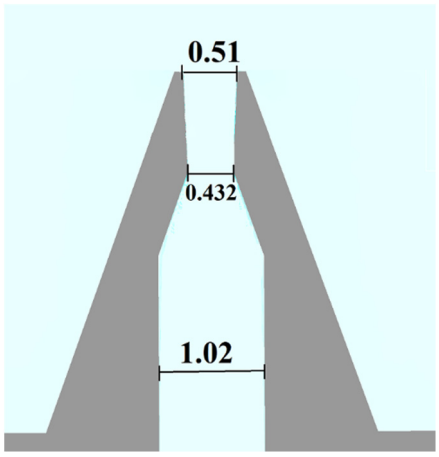

Figure 1. Nozzle geometry from minor axis plane of view, dimensions in inches.

2.3. Computational Domain and Boundary Conditions

LES with WALE subgrid-scale model is conducted as WALE accounts for both strain and rotation tensor [47]. Two operating conditions are presented as detailed in Table 2. These conditions are chosen primarily to demonstrate the budgets for ideally expanded cold jet as well as under-expanded heated jet, thus, capturing the jet behavior from budget standpoint. From here onwards, the LES cases are abbreviated as shown in Table 2. Note that Reynolds numbers based on jet exit conditions are also shown and they decrease at higher pressure and temperature ratio on account of change in dynamic viscosity, jet exit density and velocity. The computational domain extends $100 \times D_e$ downstream the nozzle exit, $15 \times D_e$ radially and $10 \times D_e$ upstream.

Table 2. LES case nomenclature.

Case Name	Jet-Exit Condition	NPR	Heated Conditions	M_j	Re_j
LEScold	Ideally expanded	3.67	Cold flow	1.5	~850,000
LEShot	Under-expanded	4	Hot flow, TR = 2.6	1.57	~350,000

Obtaining precursor converged RANS solution is crucial before launching LES case. Therefore, much attention was given to the setup of the RANS case which captured the nozzle internal wall-bounded flow and jet region. Appropriate grid refinements were used in these areas to keep y + ~1. This ensured a converged RANS with adequate quality of agreement in the results. Three volumetric grid refinement zones are used for nozzle, near-field, and velocity decay region and details are shown in Table 3. Zone I corresponds to the refinement in the nozzle, Zone II corresponds to the region spanning from nozzle exit to five diameters downstream which covers the shear layers on both minor and major axis. Zone III starts immediately after the end of Zone II and lasts 25 diameters downstream. These zones are in cylindrical frustrum shape in line with the direction of jet spread. Further details on grid refinement study can be found in our previous work [26]. LES cases were run on the two in-house HPC clusters at University of Cincinnati's Advanced Research Computing (ARC) center. *LEScold* was run on a 17-node cluster with a total of 1088 cores. Note that this is the first time such heavy computations have been conducted with massive parallelization using an in-house cluster at University of Cincinnati. *LEShot* was run on another cluster equipped with 36 compute nodes, each with 40 × 2 hyperthreaded cores. Out of the 36 nodes, only ~6–7 nodes were used for *LEShot* totaling ~560 cores which took just over 300,000 CPU-hours for completion. Further details on HPC runtime statistics for *LEScold* can be found in our previous paper [26].

Table 3. Grid refinement details.

Number of Cells (Million)	Zone I	Zone II	Zone III
73	$D_e/51$	$D_e/82$	$D_e/51$

2.4. Averaging of Flow Variables

In compressible flow, density fluctuations play an important role and, therefore, the averaging of instantaneous variables needs to be performed carefully. A density-averaged quantity follows the definition of $\frac{\overline{\rho\phi}}{\overline{\rho}}$, where an overbar denotes ensemble averaging. The instantaneous quantity is the sum of mean and fluctuating quantity which is given as $\phi = \widetilde{\phi} + \phi''$, where, $''$ denotes fluctuating part of Favre-averaged quantity and tilde denotes Favre-averaged quantity. Following this definition, Favre averaging, also known as density averaging, was performed for the conserved variables. Since Star-CCM+ does not perform Favre averaging by default settings, field functions were defined following abovementioned definition. Averaging is performed over three flow-through times for both cases, where one flow-through time is $100 \times \frac{D_e}{u_j}$.

3. Results

The initial subsections of the results present some qualitative metrics to establish a good resolution and accuracy in the numerical results, followed by an explanation on budget statistics for both LES cases. Finally, an explanation for budget residuals is provided.

3.1. Resolution of TKE

Since budget analysis involves higher-order turbulence statistics, it is imperative to obtain highly resolved flowfield. Therefore, the quality of resolved flowfield is quantified in terms of the ratio of subgrid-scale TKE to total TKE, thereby showing the percentage of the modeled TKE as compared to total TKE. The subgrid-scale TKE is expressed as

$k_{SGS} = C_t \frac{\mu_t}{\rho} S$, where C_t is the model constant and fixed at 3.5, μ_t is the turbulent viscosity, ρ is the density and S is the strain rate tensor. Figure 2 shows the ratio of subgrid-scale to total TKE and is given as $\frac{k_{SGS}}{k_{SGS}+k_R}$. It is plotted at three different downstream locations on the minor axis plane. These streamwise locations are chosen so that they fall in the potential core and mixing regions. Since the ratio is ~1–3%, it can be inferred that the LES resolves the scales reasonably.

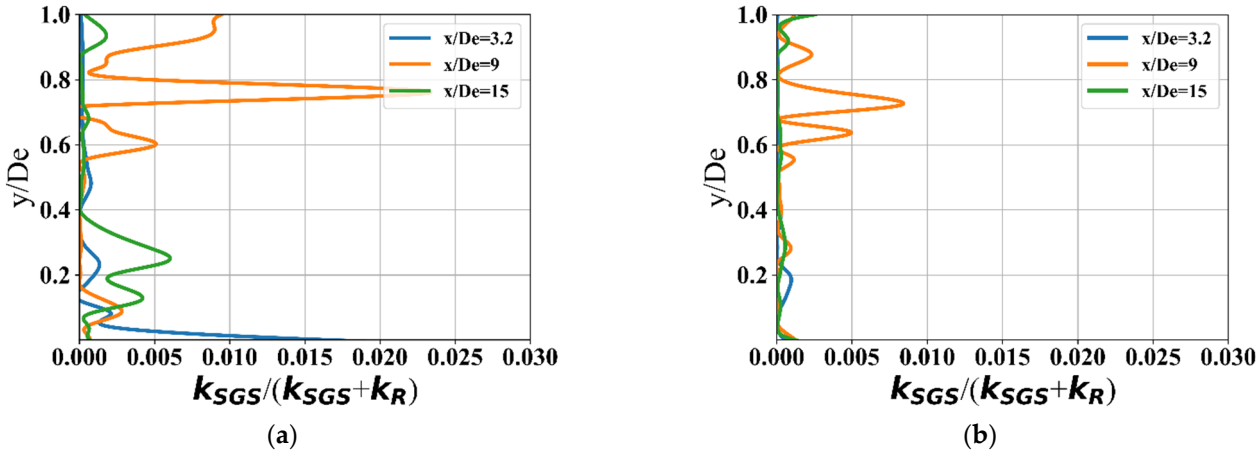

Figure 2. Ratio of subgrid-scale to total TKE at various streamwise locations. (**a**) *LEScold*—minor axis plane, (**b**) *LEShot*—minor axis plane.

3.2. Validation with PIV Experimental Data

Experimental data are reported in reference [45] and are based on PIV measurements conducted at the University of Cincinnati's Gas Dynamics Propulsion Lab. As explained by Baier et al. [45], the PIV images were taken by seeding the jet flow with 1 µm Aluminum oxide particles and ambient seeding was accomplished through olive oil droplet spray. Further details on PIV capability at the University of Cincinnati can be found in the works [45,48,49]. Since the current work only deals with numerical simulations, the details of PIV are omitted for the sake of brevity. Figure 3 shows a comparison of jet centerline velocity normalized by u_j with PIV experimental data [45].

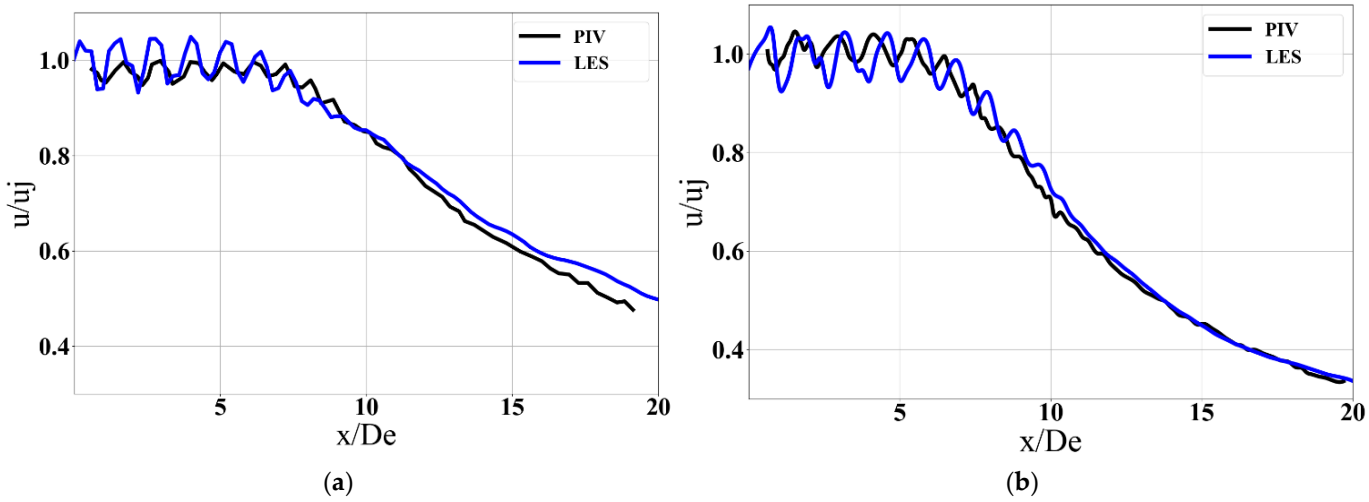

Figure 3. Normalized (by u_j) jet centerline velocity comparison with PIV experimental data from Baier et al. [45]. (**a**) *LEScold*, (**b**) *LEShot*.

As can be seen, LES captures the locations of the first few shock cells as well as the potential core damping quite accurately in Figure 3a. The amplitude of velocity oscillations

is higher as compared to experimental data. This is a result of various factors, including experimental uncertainties and numerical techniques. One explanation is the current simulations do not use synthetic turbulence at the nozzle inlet, thus, resulting in lower turbulence levels immediately downstream of the exit. While PIV is a non-intrusive technique, it suffers from uncertainties resulting from equipment, processing algorithm and particle lag, as described in references [48–51]. As mentioned by Cuppoletti [48], the experimental uncertainty in centerline velocity can be ±5%. In examining Figure 3b, it appears that shock cell locations are not coincident with each other. One explanation is the flow in this case is heated and underexpanded and particle lag through the region of shock waves can be significant, as highlighted by Lazar et al. [51]. Although these differences exist, the overall trends are captured by LES.

Figure 4a,b show the TKE comparisons with experimental data for *LEScold*. They are compared on both minor and major axis planes in the region of shear layers. Further, the TKE is normalized with u_j^2. Note that the TKE in experiments was defined using streamwise and radial components based on the assumption, $\overline{v'v'} = \overline{w'w'}$ and so, for validation purposes, this definition was used. The differences in TKE from LES and experimental data can be attributed to several factors, including the averaging time for experimental data and LES, PIV-related uncertainty in measurements and resolution of PIV, and numerical techniques, such as the discretization schemes, filtering and averaging. Further, the current work does not use synthetic turbulence generation at the nozzle inlet and results in lower turbulence immediately after the nozzle exit. A brief description on PIV-related uncertainties can be found in [48–51]. As mentioned in [48], the shear layers in supersonic jets are characterized by high velocity gradients and, therefore, this region is more prone to PIV uncertainties. Due to this fact, the agreement between experimental and LES-based TKE values improves as one moves away from the nozzle exit because the velocity gradients tend to settle down. The uncertainties in the current experimental facility were ±15% in turbulence, as mentioned in reference [48]. Assessing the individual responsible factors is beyond the scope of the present work. Although these differences exist, the agreement in terms of overall trends is decent for both minor and major axis planes and serves the purpose of validation for the broader goal of this paper. The TKE for *LEShot* conditions was not reported in experimental data and so could not be compared in this context.

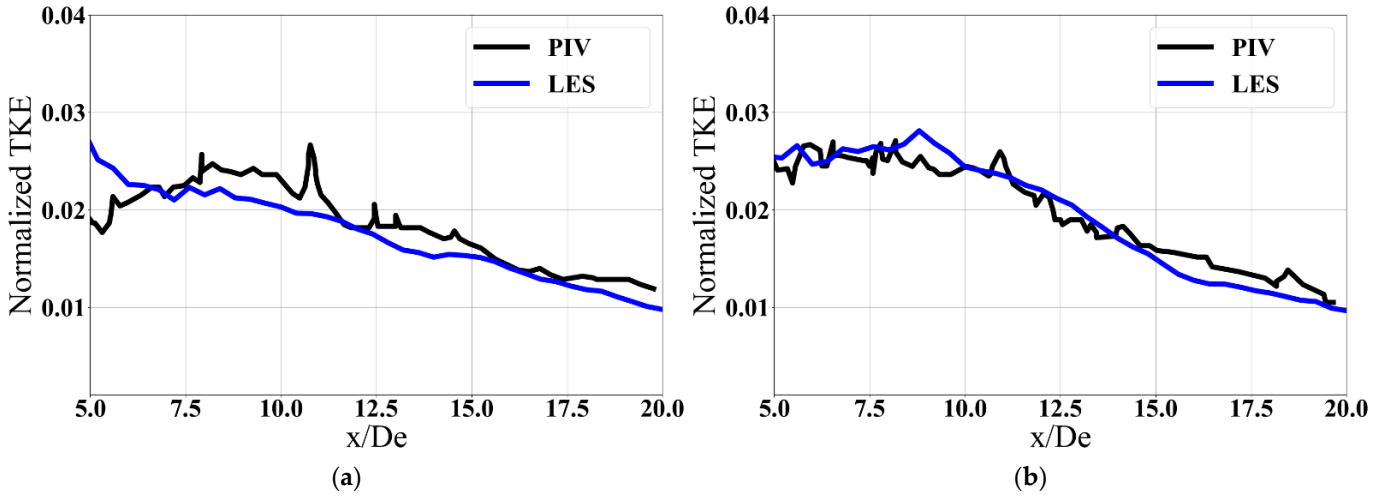

Figure 4. Normalized (by u_j^2) TKE comparison with PIV experimental data from Baier et al. [45]. (**a**) *LEScold*—minor axis plane, (**b**) *LEScold*—major axis plane.

3.3. Instantaneous Flowfield Visualization

This subsection shows the instantaneous flowfield for the *LEScold* case in Figure 5. The contours of normalized density gradient are shown below for minor and major axis

planes. The formation of shock train can be seen inside the nozzle due to the sharp throat. The shock train convects downstream of the nozzle exit. Another set of shock trains arise downstream of the nozzle exit.

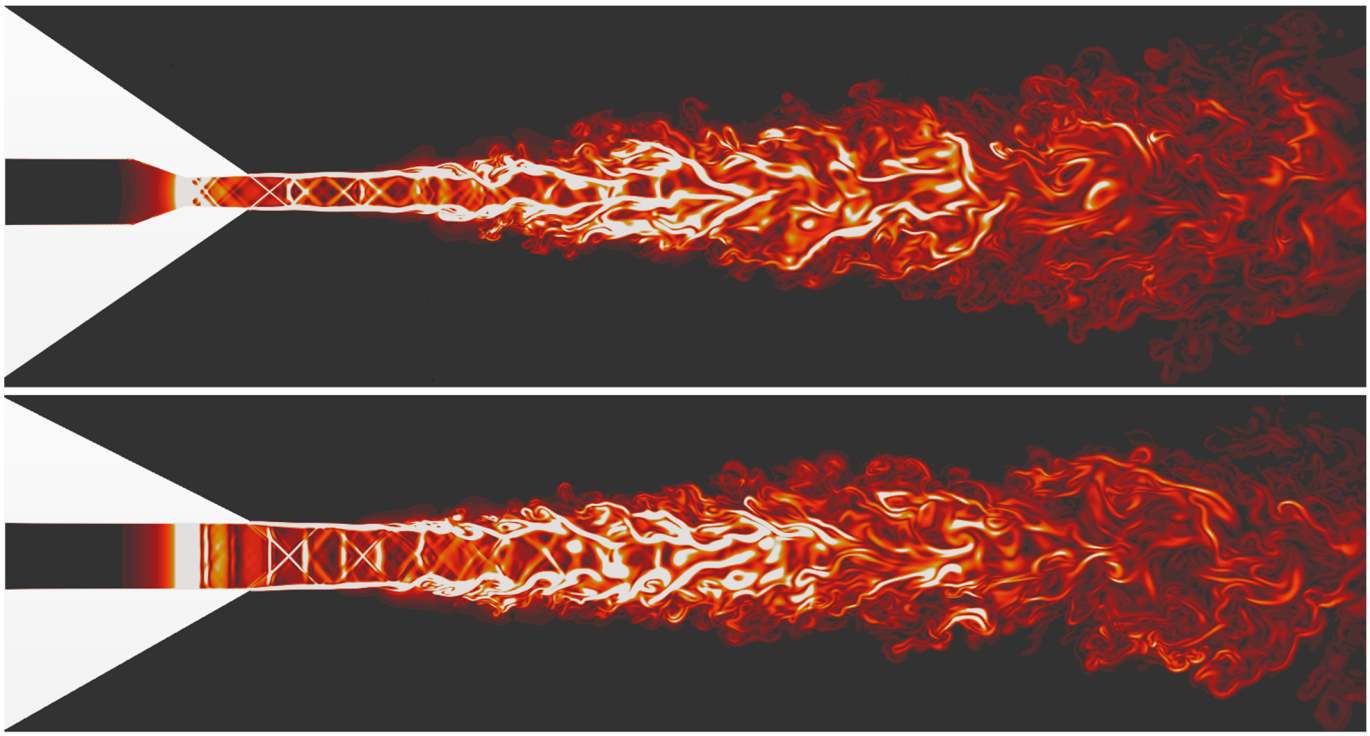

Figure 5. Contours of normalized instantaneous density gradient for *LEScold*.

3.4. Temporal Convergence of Higher-Order Statistics

This section discusses the convergence of TKE statistics based on time. Obtaining a converged solution of higher-order statistics is a direct measure of averaging time for LES solution. Inadequate computational time may lead to sporadic statistics due to the fluctuating nature of the flow and may be worse in the case of higher-order statistics. Therefore, progression of triple-velocity correlations ($\overline{\rho u_j'' u_i'' u_i''}$) and pressure-velocity correlations is assessed here at each flow-through time. Triple-velocity correlations directly affect the turbulence diffusion as their spatial gradients indicate turbulence transport, whereas pressure-velocity correlation directly affects the pressure diffusion term. Therefore, these two terms are of particular interest due to the presence of second- and third-order statistics.

Figure 6a shows the non-dimensional triple-velocity correlations for *LEShot* on the minor axis plane. They are normalized by $\rho_j u_j^3$ to obtain non-dimensional form. The location $x/D_e = 3.2$ is chosen because the budgets are at their highest magnitudes at this location for the *LEShot* case. Figure 6b shows the pressure velocity correlations for the *LEShot* case. A non-dimensional form of time is obtained and denoted by t^*. It is defined as a non-dimensional time when the Favre-averaging activity is triggered. Therefore, each t^* value can be thought of as a flow-through time. From both three-dimensional plots, it is seen that as the time progresses, the change in higher-order statistics becomes smaller, indicating their temporal convergence. Furthermore, it was ensured (Figure 7a,b) that the numerical diffusion ($\sim \Delta x^2 \frac{\partial^3 u}{\partial x^3}$) coming from second-order spatial discretization scheme was significantly lower (order of 1×10^{-8}) than the normalized value of triple-velocity correlations. Note that the numerical diffusion is plotted separately in Figure 7b since its values are quite small. This established the merits in the statistics.

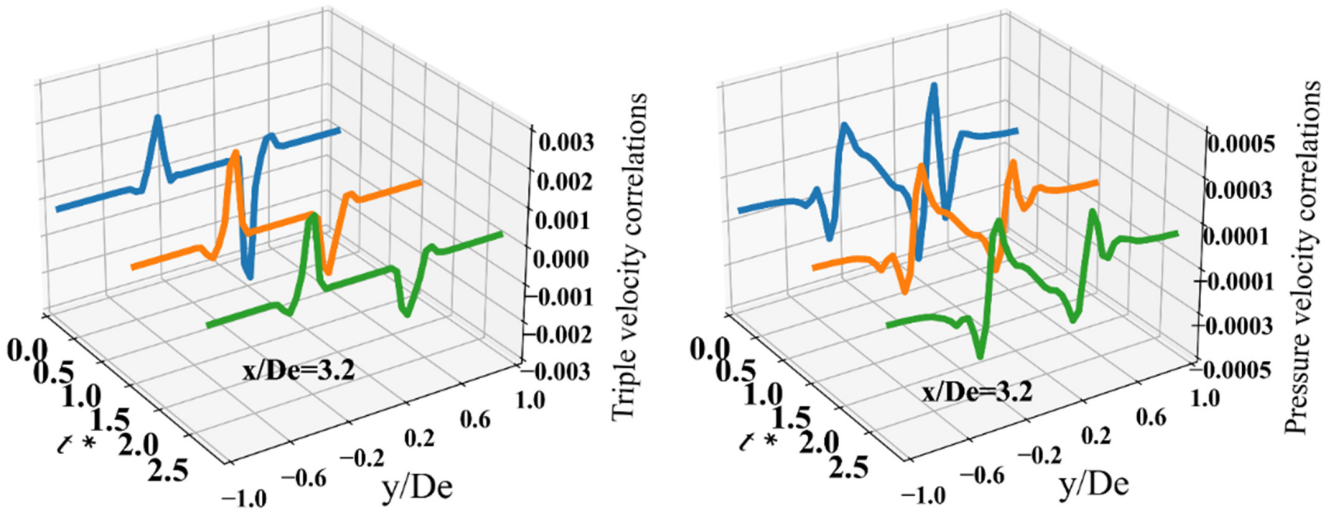

(**a**) (**b**)

Figure 6. Temporal evolution of higher-order statistics (normalized by $\rho_j u_j^3$) for *LEShot* on minor axis plane at x/D_e = 3.2. (**a**) Normalized triple-velocity correlations, (**b**) Normalized pressure-velocity correlations.

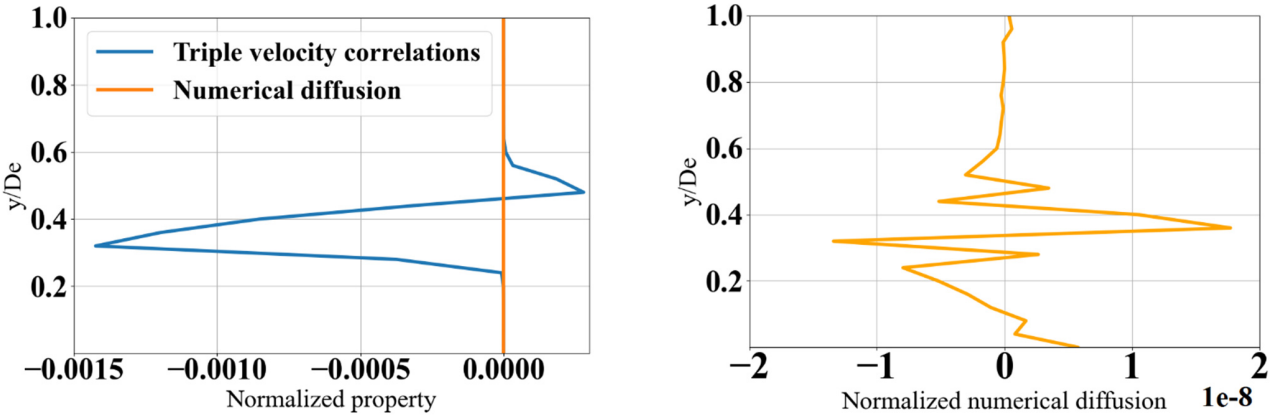

(**a**) (**b**)

Figure 7. (**a**) Comparison of normalized triple velocity correlations with normalized numerical diffusion, (**b**) Normalized numerical diffusion, at x/De = 3.2 for *LEShot*.

3.5. TKE Budgets—Before The End of Potential Core

This subsection shows the normalized TKE budgets at various streamwise locations called x/D_e, where x is the streamwise distance from the nozzle exit and D_e is the equivalent diameter at the nozzle exit. The budget terms are multiplied by $\frac{D_e}{\rho_j u_j^3}$ so that their non-dimensional form is obtained. Further, the terms with positive values are called gain and the terms with negative values are called loss. Figure 8 indicates the budget terms at three streamwise locations (x/D_e = 3.2, 4, 6) on minor and major axis planes for the *LEScold* case. These locations are chosen because the production term grows starting at x/D_e = 3.2. Since the minor axis plane corresponds to the XY plane, the statistics are calculated using gradients in the radial direction $\left(\frac{\partial}{\partial y}\right)$. Since major axis plane corresponds to the XZ plane, the gradients represent $\left(\frac{\partial}{\partial z}\right)$. For production and turbulence diffusion terms, corresponding components of velocity are used for the major axis plane. For example, production on the major axis plane is $\overline{\rho}\tau_{ik}\frac{\partial \tilde{u}_i}{\partial x_k}$. Turbulence diffusion on the major axis plane is, $-\frac{\partial}{\partial x_k}\left(\overline{\rho u_k'' \frac{1}{2} u_i'' u_i''}\right)$. Similarly, the viscous dissipation term on the major axis plane is,

$-\overline{t_{ki}\frac{\partial u_i''}{\partial x_k}}$. At x/$D_e$ = 3.2 in Figure 8a,b, the primary source is TKE production, followed by convection for Figure 8b. Since the production happens through Reynolds shear stresses as well as mean flow gradients, it represents a contribution from mean flow to turbulence. Turbulence diffusion represents the transport due to triple correlations of velocity. In the inner and outer region of the shear layer, it acts as a source term while in the central region of the shear layer, it acts as a sink. Turbulence diffusion offers a net loss in the regions of peak production. Pressure diffusion represents the transport due to pressure-velocity fluctuations. Its behavior is similar to turbulence diffusion, except with smaller magnitudes. Pressure dilatation contributes to the loss by means of fluctuating pressure and gradient of velocity fluctuation. This term is directly comparable to the production term at all three streamwise locations. Dilatation term is a direct measure of velocity gradient and pressure fluctuations. In rectangular jets, the gradients in the orthogonal direction to the streamwise direction are higher and, therefore, directly contribute to the dilatation. The pressure fluctuations are also a result of compressibility. As a result, dilatation contributes to the net loss. The production and pressure dilatation are comparable in the immediate vicinity of the nozzle, thus, indicating pronounced compressibility effects on account of shock formation in the core of the jet. Molecular diffusion represents transport on account of molecular viscosity and is negligible compared to other terms at both locations. The pressure work term is comparatively negligible. The viscous dissipation term is also insignificant. Since the stress tensor contains a resolved and subgrid-scale part, SGS diffusion and dissipation terms arise in the TKE transport equation. Their contributions are also calculated and are negligible compared to other terms, indicating that most of the TKE is resolved. From Figure 8's left- and right-hand side, it is evident that the asymmetry in TKE arises due to the production, convection, dilatation and diffusion terms for the *LEScold* case.

Figure 9 shows the budget analysis for the *LEShot* case. It is clear that TKE production due to Reynolds shear stresses has the highest contribution. The region of peak production aligns with the region of peak turbulence diffusion at x/De = 3.2. The turbulence diffusion reaches its peak in the central part of the shear layer rather than the outer edges. This indicates that towards the outer edges, the velocity fluctuations transport the TKE causing the turbulence gain. Therefore, the turbulence diffusion contributes to the loss in the central region while it acts as a source towards the outer edges of the shear layer. The pressure dilatation term contributes to the loss throughout the growth of the jet.

A noticeable difference between Figures 8 and 9 is due to the levels of production and pressure dilatation terms. In Figure 9, the production term is the highest at x/D_e = 3.2 while the dilatation term is comparatively lower than in corresponding location in Figure 8. The TKE is gained at the jet centerline, just before the end of the potential core on account of turbulence diffusion on the minor axis plane in Figure 8e. This happens first on the minor axis plane due to the merging of shear layers and later on the major axis plane since the shear layers are further apart due to the nozzle-exit aspect ratio. It directly affects the growth of shear layers on the major axis plane, thus, causing them to develop apart. From both figures, it is evident that production, turbulence diffusion and pressure dilatation provide significant contributions, followed by convection and pressure diffusion.

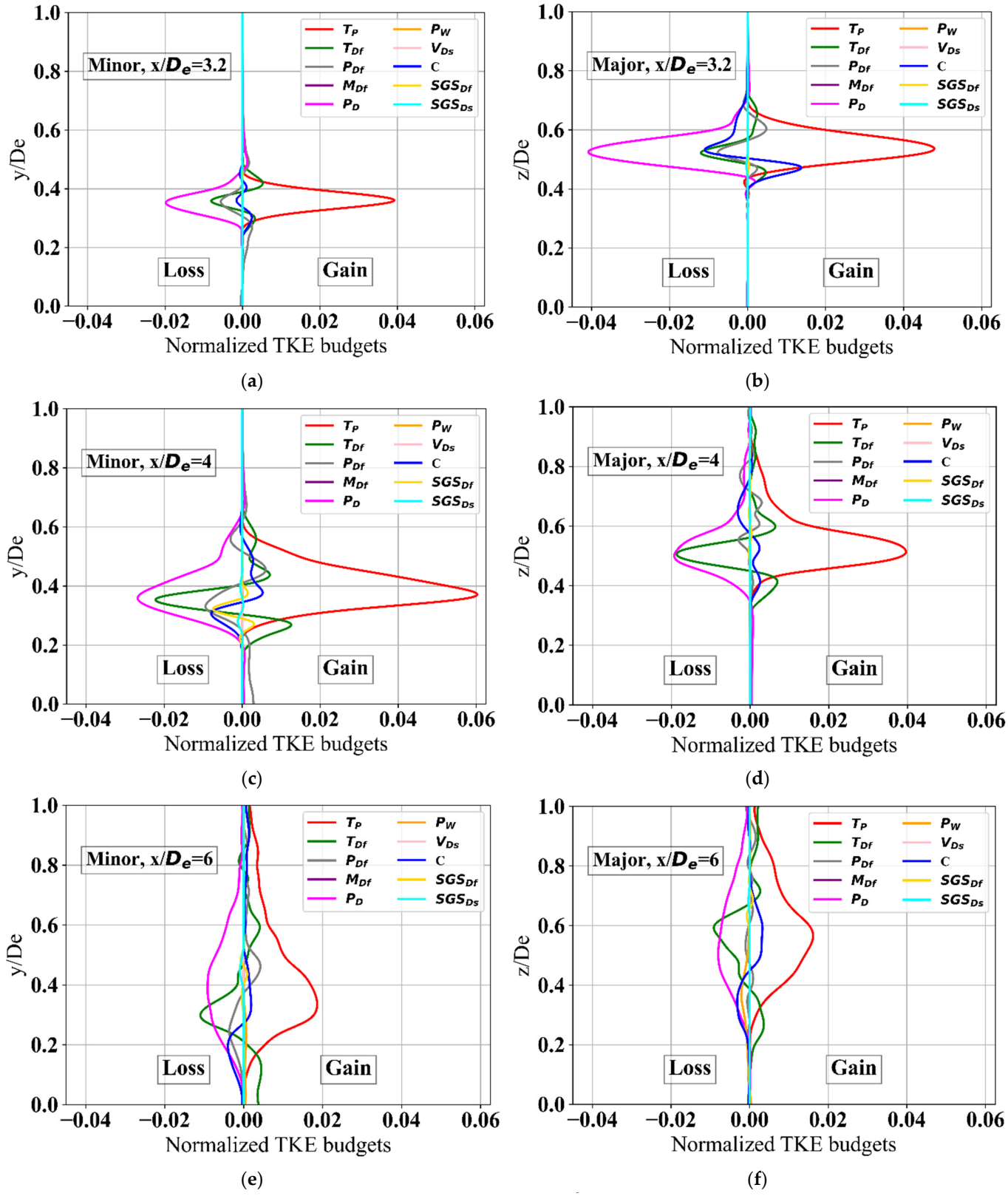

Figure 8. TKE budgets (normalized by $\frac{\rho_j u_j^3}{D_e}$) for *LEScold*. (**a**) x/De = 3.2—minor axis, (**b**) x/De = 3.2—major axis, (**c**) x/De = 4—minor axis, (**d**) x/De = 4—major axis, (**e**) x/De = 6—minor axis, (**f**) x/De = 6—major axis.

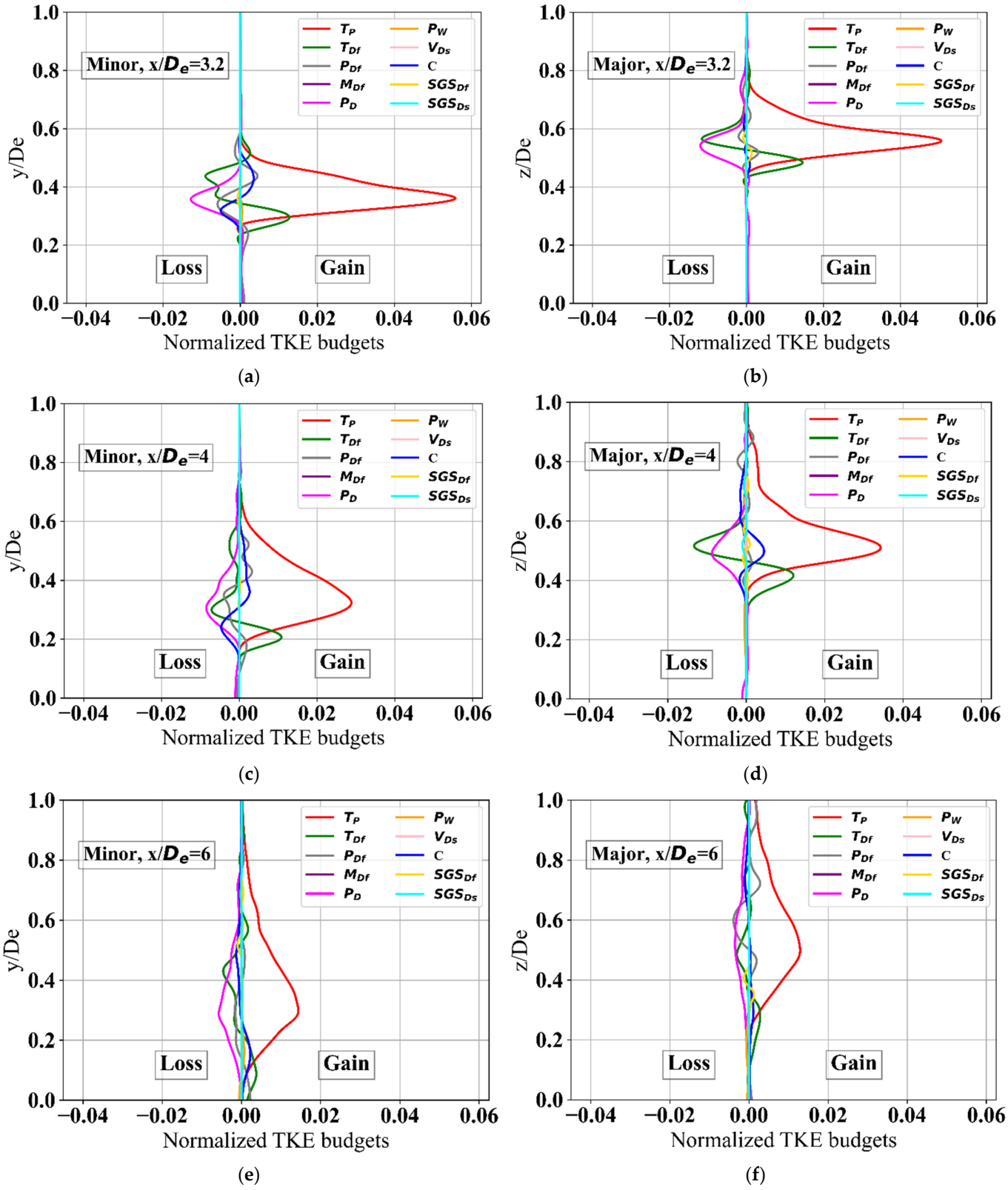

Figure 9. TKE budgets (normalized by $\frac{\rho_j u_j^3}{D_e}$) for *LEShot*. (**a**) x/De = 3.2—minor axis, (**b**) x/De = 3.2—major axis, (**c**) x/De = 4—minor axis, (**d**) x/De = 4—major axis, (**e**) x/De = 6—minor axis, (**f**) x/De = 6—major axis.

3.6. TKE Budgets—After the End of Potential Core

This section highlights what happens after the end of potential core. Figure 10 shows the budgets for *LEScold* at x/D_e = 9, 12 on minor and major axis planes. These two locations are chosen because they are immediately after the end of potential core, where the mixing is a dynamic process. The major source and sink are from production and dilatation term. The turbulence diffusion on the minor axis plane at x/D_e = 9 is visible from Figure 10a. This is due to the merging of shear layers on the minor axis plane compared to the major axis plane. Further downstream, the turbulence diffusion towards the jet centerline at x/D_e = 12 becomes greater as compared to its minor axis counterpart. This is because of the merging of shear layers at a later stage. In Figure 10a,b, the TKE convection is evident, whereas, as one moves towards x/D_e = 12, the convection becomes smaller since the potential core has fully damped out at this location.

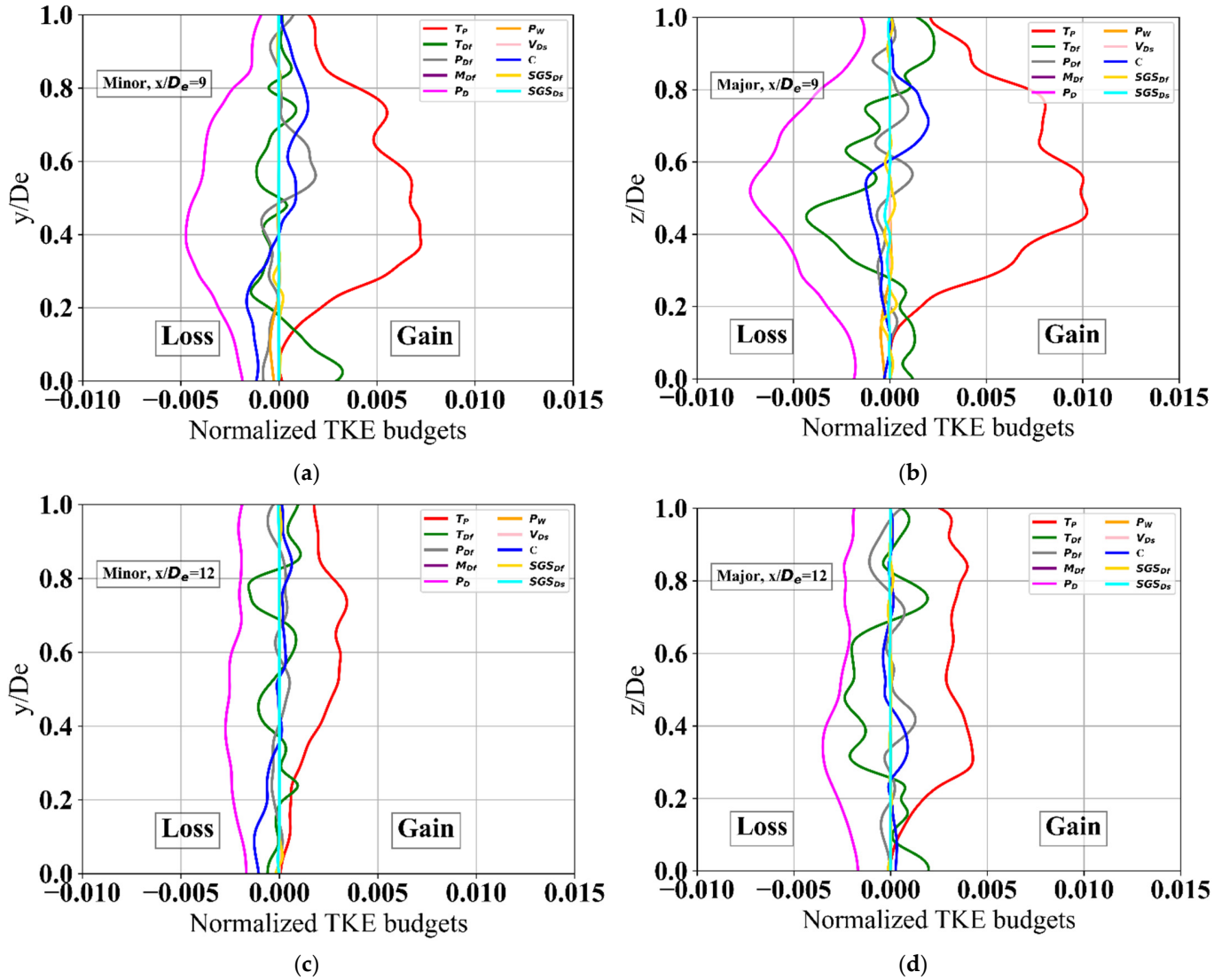

Figure 10. TKE budgets (normalized by $\frac{\rho_j u_j^3}{D_e}$) for *LEScold*. (**a**) x/De = 9—minor axis, (**b**) x/De = 9—major axis, (**c**) x/De = 12—minor axis, (**d**) x/De = 12—major axis.

Figure 11 shows the same for the *LEShot* case, where production, diffusion and pressure dilatation play a major role. Since these locations fall in the mixing region, the overall budget magnitudes decrease.

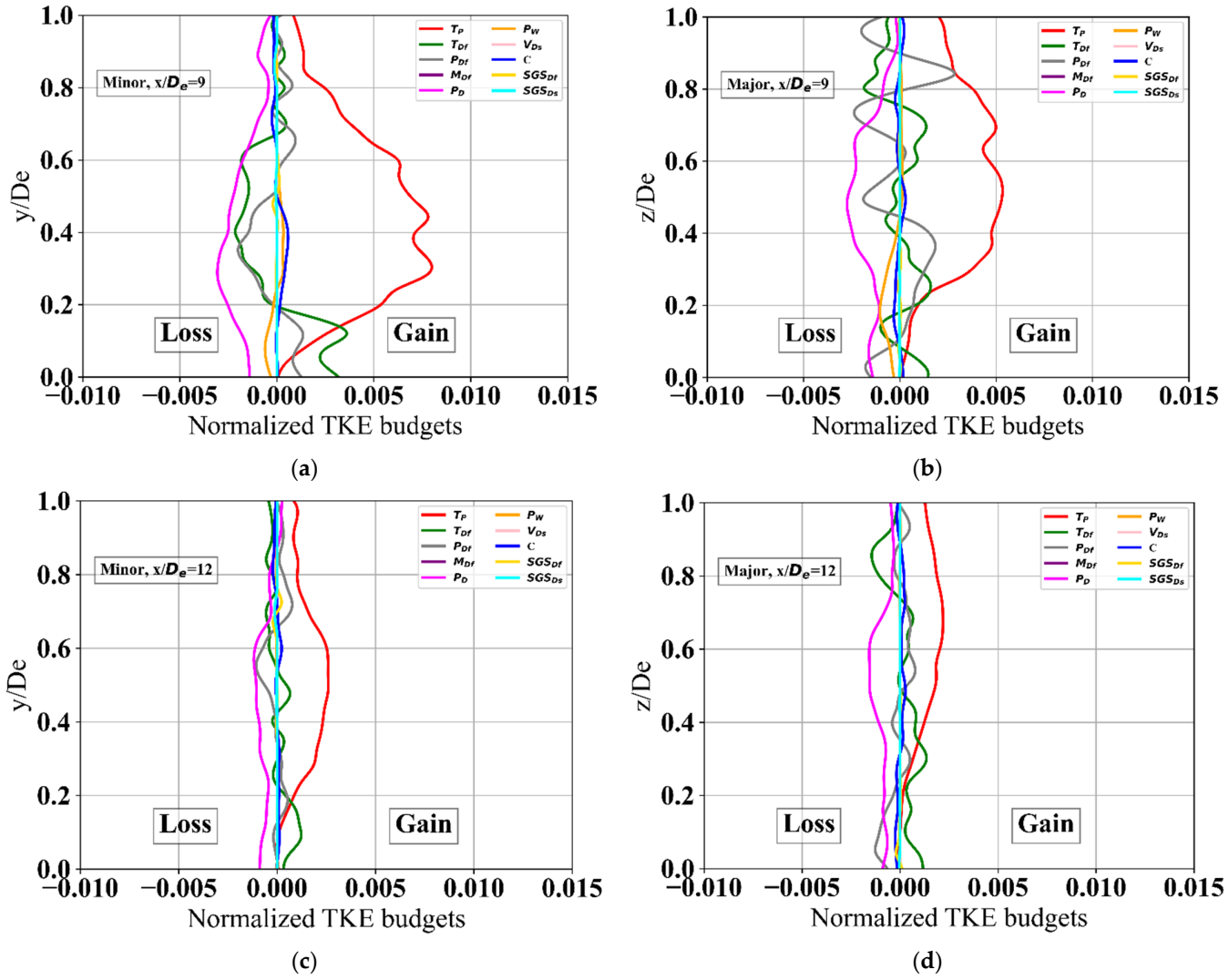

Figure 11. TKE budgets (normalized by $\frac{\rho_j u_j^3}{D_e}$) for *LEShot*. (**a**) x/De = 9—minor axis, (**b**) x/De = 9—major axis, (**c**) x/De = 12—minor axis, (**d**) x/De = 12—major axis.

3.7. Temporal Evolution of Budget Residuals

Theoretically, the balance of all terms in the TKE transport equation should be zero due to the conservation of energy. However, numerically, it may not be so, and their balance can be thought of as a residual. Several factors affect the residual term and its value. The goal of this subsection is to explain the residual term in the TKE budget equation. As mentioned previously, since the residual is calculated as the balance of budget terms, its value is a combined effect of many factors, such as the spatial discretization schemes, temporal discretization schemes, LES grid, LES filtering activity, total averaging time for the numerical simulation and statistical convergence of numerical simulations. Assessing the individual factors is beyond the scope of the current work. However, an explanation is provided here as to how the residual term develops in time. Therefore, in order to examine its time-dependent evolution, three-dimensional plots are shown in Figures 12 and 13 for *LEScold* and *LEShot*, respectively. A non-dimensional time denoted as t^* represents a flow-through time after the budget-averaging activity is triggered. The plot reveals the residual term at certain time steps as the solution progresses in time. Note that for *LEScold*, the terms are positive and negative at various downstream locations. This behavior stems from the peak values of local production and dilatation terms, whereas for *LEShot*, it is primarily negative. A positive value represents a local gain while negative value represents

a local loss. The residual should be as close to zero as possible, thus, indicating a good balance of all terms. In present work, the residuals are highest in the immediate vicinity of the nozzle exit. From both figures, it is evident that when the averaging activity is triggered ($t^* \sim 0$), the residuals are at their highest values but as the solution progresses in time ($t^* > 2$), their values decrease on account of settling down. In examining Figures 12 and 13, the magnitudes of residuals at $x/D_e = 3.2$ are quite different. This is because the peak budget values are reached at different streamwise locations on *LEScold* and *LEShot*. In *LEScold*, the peak of production term is at $x/D_e = 4$ while for *LEShot* the peak is at x/De = 3.2. Similarly, the peaks of pressure dilatation terms differ in both cases. *LEScold* is characterized by a stronger dilatation effect compared to *LEShot* in the streamwise locations closer to the nozzle exit. Further, the turbulence diffusion term for *LEScold* at this location (Figure 8a,b) is lower and becomes comparable to the dilatation term further downstream. As a result, the residual term in *LEScold* shows different trends (at $x/D_e = 3.2$) than that of *LEShot*. The results also differ due to the behavior of each term on minor and major axis planes on upper and lower shear layers. Also, the TKE production term shows different peaks on minor and major axis planes of *LEScold* (Figure 8a,b). Comparing the residual term with other budget terms, it is clear that the peak value of the residual term is less than the peak value of production term. The net balance of the TKE budget equation terms was also reported in previous works. However, the terminology was different. In references [7,8], the filtering dissipation was calculated as the balance of all budget terms and their values were of the same order of magnitude as the production term.

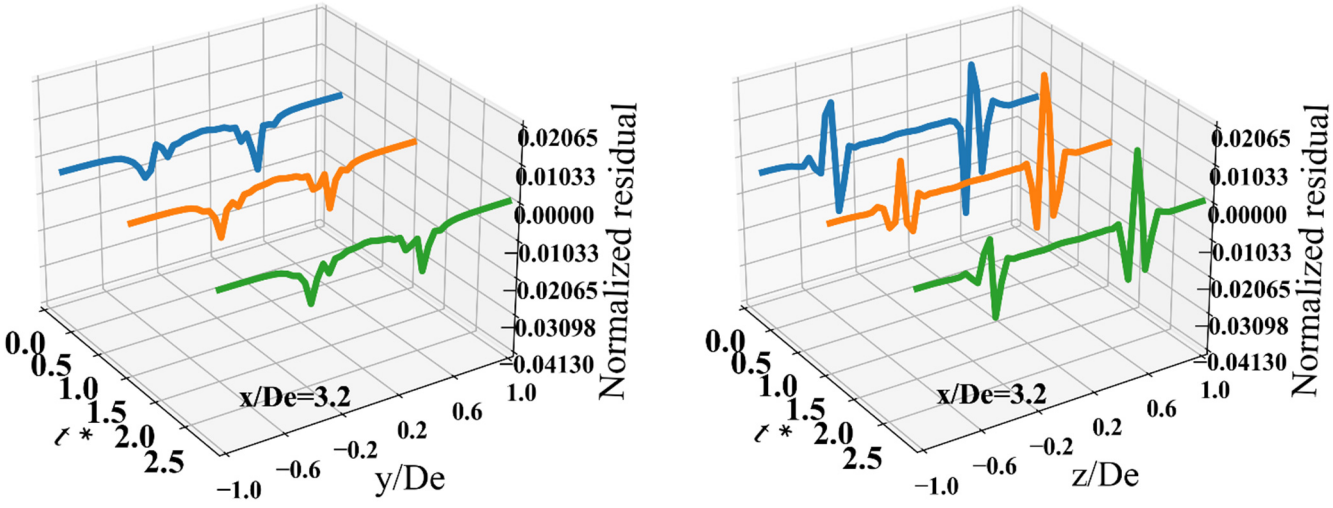

Figure 12. *Cont.*

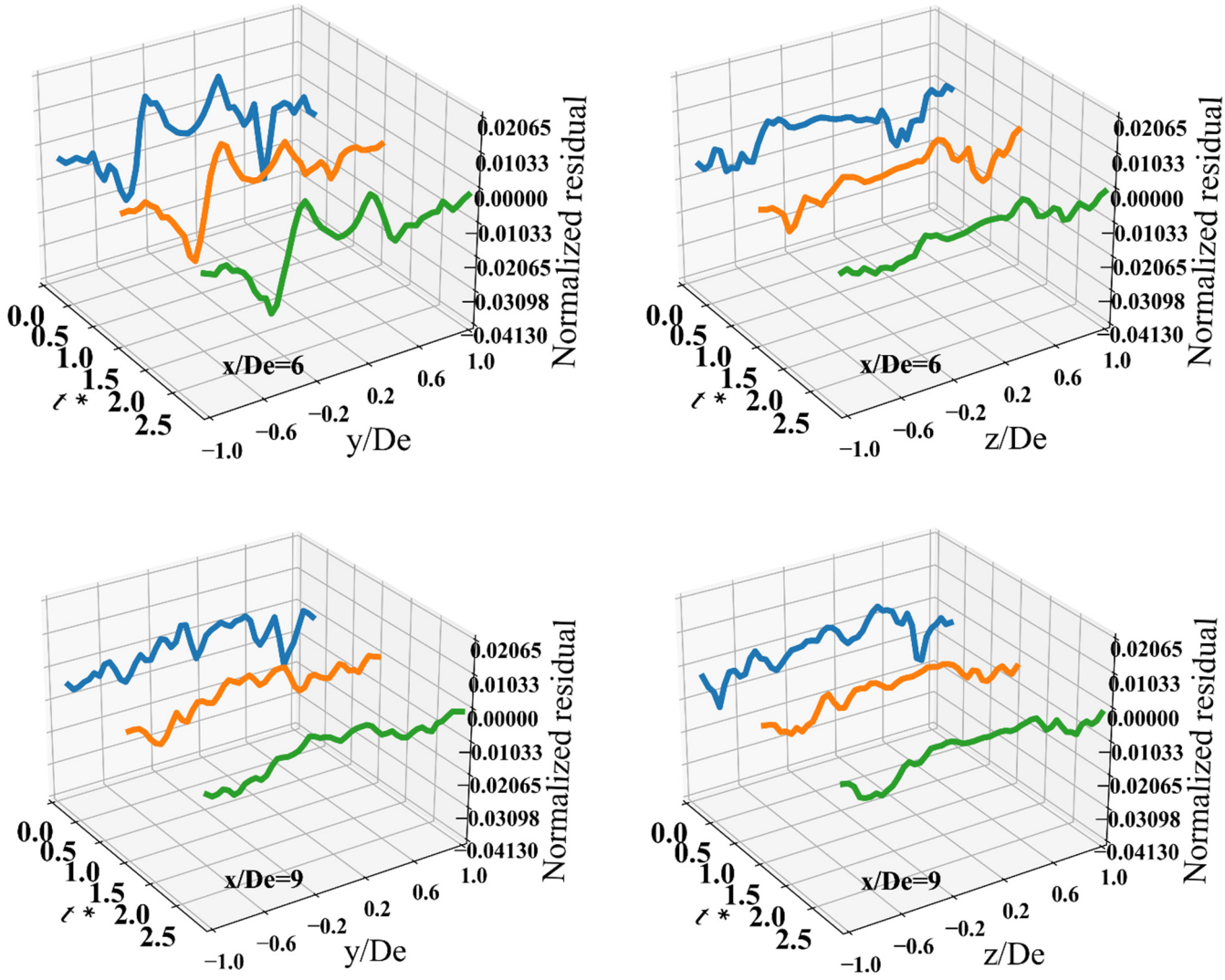

Figure 12. Temporal evolution of budget residuals (normalized by $\frac{\rho_j u_j^3}{D_e}$) along streamwise locations x/D_e = 3.2, 6, 9—left: *LEScold* minor, right: *LEScold* major.

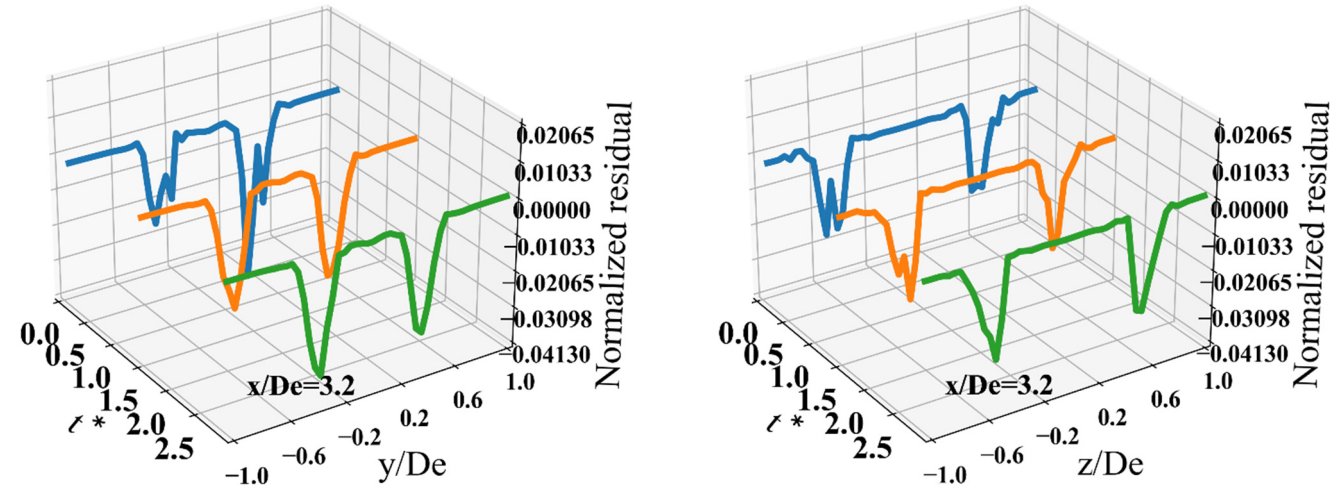

Figure 13. *Cont.*

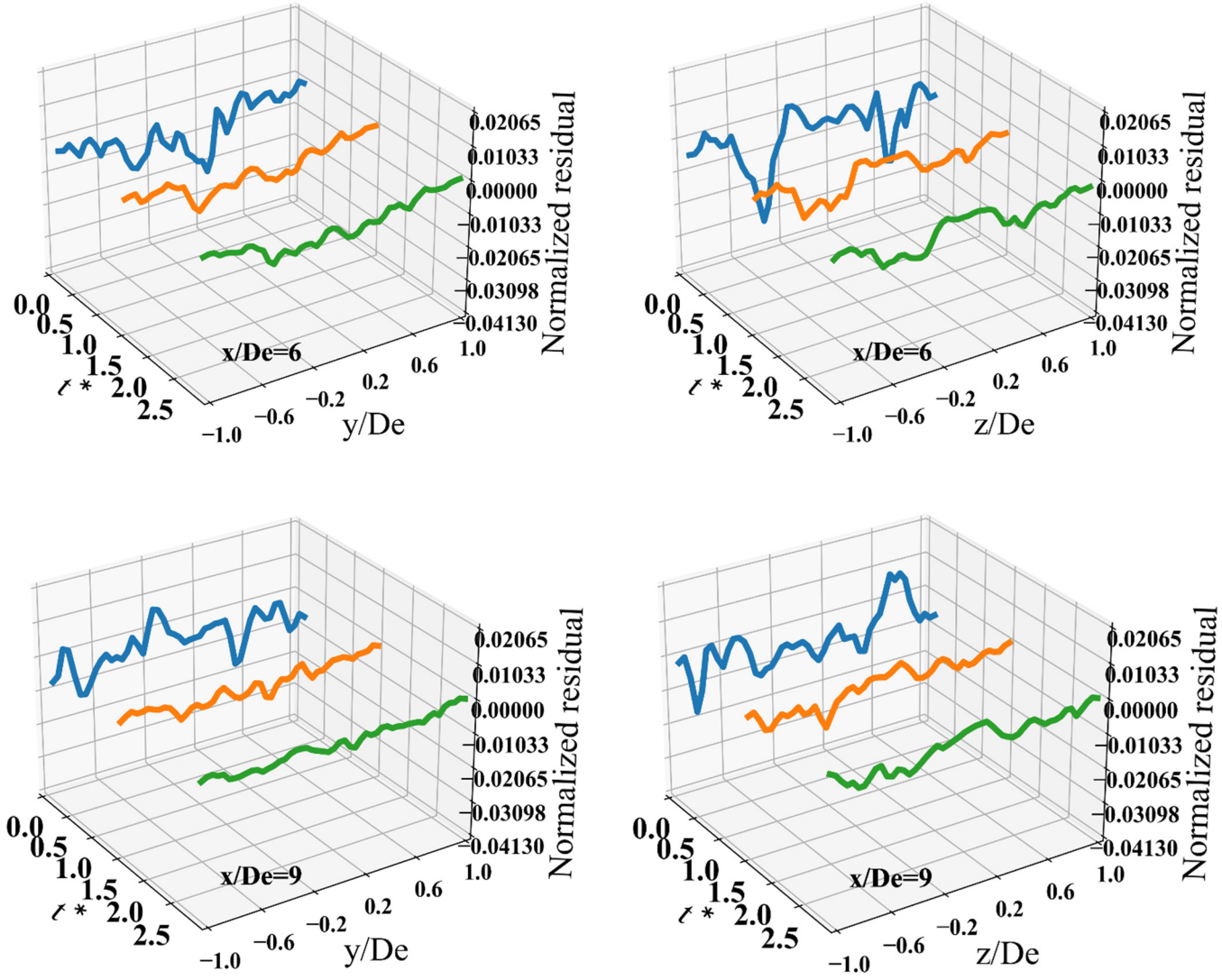

Figure 13. Temporal evolution of budget residuals (normalized by $\frac{\rho_j u_j^3}{D_e}$) along streamwise locations x/De = 3.2, 6, 9—left: *LEShot* minor, right: *LEShot* major.

4. Conclusions and Future Work

The primary objective of this paper is to examine the rectangular jet flowfield from a TKE budget standpoint to highlight the turbulence transport mechanisms during jet development and mixing. As a result, the anisotropic TKE budgets are demonstrated for rectangular jets for the first time. The results are presented for an ideally expanded cold jet and under-expanded heated jet. To gain access to all components in the TKE transport equation, Large Eddy Simulations are conducted. The subgrid-scale turbulence is modeled using WALE model. Various spatial and temporal metrics of convergence are used to ensure the convergence of higher-order statistics as well as to ensure a good resolution of TKE. The jet nearfield results are validated with PIV experimental data. The centerline velocity is predicted accurately by LES, which captures the location of the first few shock cells and the potential core-damping region quite well. The TKE on minor and major axis planes is also validated with PIV data from literature. LES captures the overall trends in TKE. A brief explanation is provided on the factors causing the differences between the TKE magnitudes in experiments and numerical simulations. Evaluation of these factors is beyond the scope of the present work since LES captured the overall trends correctly.

As part of budget analysis, it is shown that TKE production is a major source term throughout the development and mixing region of a jet. The production stems from

Reynolds stresses as well as mean flow gradients and indicates gain in turbulence from mean flow. The second major contribution is from the pressure dilatation term. Turbulence diffusion arises from triple correlations of velocity. This term acts as a sink in the regions of peak production. As the potential core approaches, the turbulence diffusion peaks at the jet centerline on account of the merging of shear layers. This phenomenon occurs first on the minor axis plane and then on the major axis plane. Pressure diffusion has a similar behavior as the turbulence diffusion term. Other terms in the budget equation are comparatively insignificant in their contributions. For example, viscous and subgrid-scale dissipation, molecular and subgrid-scale diffusion are minimal throughout the growth. The residual term is calculated as a balance of other terms in the TKE equation. An explanation is provided based on temporal evolution of the residual term. Overall, the asymmetry in minor and major axis statistics mainly stems from the production, dilatation and turbulence diffusion terms, followed by convection and pressure diffusion.

Finally, this paper presented all terms in the TKE budget equation for rectangular supersonic jets for the first time. This ultimately shed some light on turbulence in supersonic flow and the contributions of various mechanisms in the local and global transport of turbulent kinetic energy and its anisotropy during jet development and turbulent mixing. The future work will be focused on improving the accuracy of numerical simulations using higher-order discretization schemes as well as addressing the internal flow physics by incorporating inflow turbulence.

Author Contributions: Conceptualization, K.B.; Data curation, K.B.; Formal analysis, K.B.; Investigation, K.B.; Methodology, K.B. and S.A.; Project administration, S.A.; Resources, S.A.; Software, S.A.; Supervision, S.A.; Validation, K.B.; Visualization, K.B.; Writing—Original draft, K.B.; Writing—Review and editing, K.B. and S.A. All authors have read and agreed to the published version of the manuscript.

Funding: This research received no funding.

Institutional Review Board Statement: Not applicable.

Informed Consent Statement: Not applicable.

Data Availability Statement: Not applicable.

Acknowledgments: The first author gratefully acknowledges partial computational resources through research cyber-infrastructure resources and services provided by the Advanced Research Computing (ARC) center at the University of Cincinnati, Cincinnati, OH, USA. Kiran Siddappaji is acknowledged for invaluable discussions on flow physics and qualitative analysis.

Conflicts of Interest: The authors declare no conflict of interest.

Abbreviations

AR	Aspect ratio
CFD	Computational fluid dynamics
CPU	Central processing unit
DNS	Direct numerical simulation
ESFR	Energy stable flux reconstruction
FD	Finite difference
FV	Finite volume
HPC	High performance computing
LES	Large Eddy Simulation
PIV	Particle image velocimetry
TKE	Turbulent Kinetic Energy
RANS	Reynolds Averaged Navier Stokes
MUSCL	Monotone upstream-centered schemes
NPR	Nozzle pressure ratio
SST	Shear Stress Transport
WALE	Wall-adapting local eddy viscosity

D_e	Nozzle-exit equivalent diameter
u	Axial component of velocity
u_j	Jet velocity at nozzle exit
ρ_j	Jet density at nozzle exit
C	Convection
T_P	TKE production
T_{Df}	Turbulence diffusion
M_{Df}	Molecular diffusion
M_j	Jet Mach number at nozzle exit
P_{Df}	Pressure diffusion
P_D	Pressure dilatation
P_W	Pressure work
V_{Ds}	Viscous dissipation
SGS_{Df}	Subgrid-scale diffusion
SGS_{Ds}	Subgrid-scale dissipation
R	Residual
Re_j	Jet Reynolds number
k_{SGS}	Subgrid-scale TKE
k_R	Resolved TKE
SGS	Subgrid scale
$'$	Fluctuation in Reynolds averaged quantity
$''$	Fluctuation in Favre averaged quantity
$\sim$	Favre-averaged quantity
-	Reynolds averaged quantity

References

1. Wilcox, D.C. *Turbulence Modeling for CFD*; DCW Industries: La Canada, CA, USA, 1998; Volume 2.
2. Gutmark, E.; Wygnanski, I. The planar turbulent jet. *J. Fluid Mech.* **1976**, *73*, 465–495. [CrossRef]
3. Nishino, K.; Samada, M.; Kasuya, K.; Torii, K. Turbulence statistics in the stagnation region of an axisymmetric impinging jet flow. *Int. J. Heat Fluid Flow* **1996**, *17*, 193–201. [CrossRef]
4. Cavo, A.; Lemonis, G.; Panidis, T. Experimental investigation of the energy budget and enstrophy in the near field of a rectangular turbulent jet. In *Turbulence Heat and Mass Transfer 6. Proceedings of the Sixth International Symposium on Turbulence Heat and Mass Transfer*; Begel House Inc.: Rome, Italy, 2009.
5. Liu, X.; Thomas, F.O. Measurement of the turbulent kinetic energy budget of a planar wake flow in pressure gradients. *Exp. Fluids* **2004**, *37*, 469–482. [CrossRef]
6. Bogey, C.; Bailly, C. Turbulence and energy budget in a self-preserving round jet: Direct evaluation using large eddy simulation. *J. Fluid Mech.* **2009**, *627*, 129–160. [CrossRef]
7. Bogey, C.; Bailly, C. Large eddy simulations of transitional round jets: Influence of the Reynolds number on flow development and energy dissipation. *Phys. Fluids* **2006**, *18*, 065101. [CrossRef]
8. Bonelli, F.; Viggiano, A.; Magi, V. High-speed turbulent gas jets: An LES investigation of Mach and Reynolds number effects on the velocity decay and spreading rate. *Flow Turbul. Combust.* **2021**, *107*, 519–550. [CrossRef]
9. Vyas Manan, A.; Waindim, M.; Gaitonde, D.V. Budget of Turbulent Kinetic Energy in a Shock Wave/Boundary-layer Interaction. In Proceedings of the 46th AIAA Fluid Dynamics Conference, Washington, DC, USA, 13–17 June 2016; p. 3187.
10. Kokkinakis, I.W.; Drikakis, D.; Ritos, K.; Spottswood, S.M. Direct numerical simulation of supersonic flow and acoustics over a compression ramp. *Phys. Fluids* **2020**, *32*, 066107. [CrossRef]
11. Orlandi, P.; Pirozzoli, S. Secondary Flow in Smooth and Rough Turbulent Circular Pipes: Turbulence Kinetic Energy Budgets. *Fluids* **2021**, *6*, 448. [CrossRef]
12. Tian, G.; Conan, B.; Calmet, I. Turbulence-Kinetic-Energy Budget in the Urban-Like Boundary Layer Using Large-Eddy Simulation. *Boundary-Layer Meteorol.* **2020**, *178*, 201–223. [CrossRef]
13. Watanabe, T.; Sakai, Y.; Nagata, K.; Ito, Y. Large eddy simulation study of turbulent kinetic energy and scalar variance budgets and turbulent/non-turbulent interface in planar jets. *Fluid Dyn. Res.* **2016**, *48*, 021407. [CrossRef]
14. Lai, C.C.K.; Socolofsky, S.A. Budgets of turbulent kinetic energy, Reynolds stresses, and dissipation in a turbulent round jet discharged into a stagnant ambient. *Environ. Fluid Mech.* **2018**, *19*, 349–377. [CrossRef]
15. Zhang, J.A.; Drennan, W.; Black, P.G.; French, J.R. Turbulence Structure of the Hurricane Boundary Layer between the Outer Rainbands. *J. Atmos. Sci.* **2009**, *66*, 2455–2467. [CrossRef]
16. Wu, Y.; Porté-Agel, F. Atmospheric turbulence effects on wind-turbine wakes: An LES study. *Energies* **2012**, *5*, 5340–5362. [CrossRef]

17. Zippel, S.F.; Farrar, J.T.; Zappa, C.J.; Plueddemann, A.J. Parsing the Kinetic Energy Budget of the Ocean Surface Mixed Layer. *Geophys. Res. Lett.* **2022**, *49*, e2021GL095920. [CrossRef] [PubMed]
18. Balakumar, P.; Rubinstein, R.; Rumsey, C.L. DNS, Enstrophy Balance, and the Dissipation Rate Equation in a Separated Turbulent Channel Flow. In Proceedings of the 21st AIAA Computational Fluid Dynamics Conference, San Diego, CA, USA, 24–27 June 2013; p. 2723.
19. Siddappaji, K.; Turner, M. Improved Prediction of Aerodynamic Loss Propagation as Entropy Rise in Wind Turbines Using Multifidelity Analysis. *Energies* **2022**, *15*, 3935. [CrossRef]
20. Siddappaji, K.; Turner, M. Multifidelity Analysis of a Solo Propeller: Entropy Rise Using Vorticity Dynamics and Kinetic Energy Dissipation. *Fluids* **2022**, *7*, 177. [CrossRef]
21. Siddappaji, K. On the Entropy Rise in General Unducted Rotors using Momentum, Vorticity and Energy Transport. Ph.D. Thesis, University of Cincinnati, Cincinnati, OH, USA, 2018.
22. Siddappaji, K.; Turner, M.G. Versatile Tool for Parametric Smooth Turbomachinery Blades. *Aerospace* **2022**, accepted.
23. Gao, F. Advanced Numerical Simulation of Corner Separation in a Linear Compressor Cascade. Ph.D. Thesis, Ecole Centrale de Lyon, Lyon, France, 2014.
24. Monier, J.-F.; Boudet, J.; Caro, J.; Shao, L. Budget Analysis of Turbulent Kinetic Energy in a Tip-Leakage Flow of a Single Blade: RANS Vs Zonal LES. In Proceedings of the 12th European Conference on Turbomachinery Fluid Dynamics & Thermodynamics, Stockholm, Sweden, 3–7 April 2017.
25. Chen, H.; Turner, M.G.; Siddappaji, K.; Mahmood, S.M.H. Flow Diagnosis and Optimization Based on Vorticity Dynamics for Transonic Compressor/Fan Rotor. *Open J. Fluid Dyn.* **2017**, *7*, 40. [CrossRef]
26. Bhide, K.; Siddappaji, K.; Abdallah, S.; Roberts, K. Improved Supersonic Turbulent Flow Characteristics Using Non-Linear Eddy Viscosity Relation in RANS and HPC-Enabled LES. *Aerospace* **2021**, *8*, 352. [CrossRef]
27. Bhide, K.R.; Abdallah, S. Turbulence statistics of supersonic rectangular jets using Reynolds Stress Model in RANS and WALE LES. In Proceedings of the AIAA AVIATION 2022 Forum, Chicago, IL, USA, Virtual, 27 June–1 July 2022; p. 3344.
28. Morkovin, M. Effects of compressibility on turbulent flow. In *The Mechanics of Turbulence*; Favre, A., Ed.; Gordon and Breach: Philadelphia, PA, USA, 1962; pp. 367–380.
29. Bradshaw, P. Compressible Turbulent Shear Layers. *Annu. Rev. Fluid Mech.* **1977**, *9*, 33–52. [CrossRef]
30. Bogey, C.; Bailly, C. Computation of a high Reynolds number jet and its radiated noise using large eddy simulation based on explicit filtering. *Comput. Fluids* **2005**, *35*, 1344–1358. [CrossRef]
31. Brès, G.; Ham, F.E.; Nichols, J.W.; Lele, S.K. Unstructured Large-Eddy Simulations of Supersonic Jets. *AIAA J.* **2017**, *55*, 1164–1184. [CrossRef]
32. Karami, S.; Stegeman, P.; Ooi, A.; Soria, J. High-order accurate large-eddy simulations of compressible viscous flow in cylindrical coordinates. *Comput. Fluids* **2019**, *191*, 104241.
33. Eliasson, P. *EDGE: A Navier-Stokes Solver for Unstructured Grids. FOI-Swedish Defence Research Agency, Division of Aeronautics*; FOI: Stockholm, Sweden, 2001.
34. Zhang, H.; Li, Y.; Xiao, J.; Jordan, T. Large eddy simulations of the all-speed turbulent jet flow using 3-D CFD code GASFLOW-MPI. *Nucl. Eng. Des.* **2018**, *328*, 134–144. [CrossRef]
35. López, M.R.; Sheshadri, A.; Bull, J.R.; Economon, T.D.; Romero, J.; Watkins, J.E.; Williams, D.M.; Palacios, F.; Jameson, A.; Manosalvas, D.E. Verification and Validation of HiFiLES: A High-Order LES unstructured solver on multi-GPU platforms. In Proceedings of the 32nd AIAA Applied Aerodynamics Conference, Atlanta, GA, USA, 16–20 June 2014; p. 3168.
36. Kailasanath, K.; Corrigan, A.T.; Liu, J.; Ramamurti, R. Efficient supersonic jet noise simulations using JENRE. In Proceedings of the 50th AIAA/ASME/SAE/ASEE Joint Propulsion Conference, Cleveland, OH, USA, 28–30 July 2014; p. 3740.
37. Kiris, C.C.; Housman, J.A.; Barad, M.F.; Brehm, C.; Sozer, E.; Moini-Yekta, S. Computational framework for Launch, Ascent, and Vehicle Aerodynamics (LAVA). *Aerosp. Sci. Technol.* **2016**, *55*, 189–219. [CrossRef]
38. Stich, G.D.; Ghate, A.S.; Housman, J.A.; Kiris, C.C. Wall Modeled Large Eddy Simulations for NASA's jet noise consensus database of single-stream, round, convergent jets. In Proceedings of the AIAA SCITECH 2022 Forum, San Diego, CA, USA, 3–7 January 2022; p. 0684.
39. Aprovitola, A.; Denaro, F.M. Using symbolic computation software packages in production of multidimensional finite volume-based large eddy simulation codes. *Int. J. Numer. Methods Fluids* **2012**, *71*, 562–583.
40. Weller, H.G.; Tabor, G.; Jasak, H.; Fureby, C. A tensorial approach to computational continuum mechanics using object-oriented techniques. *Comput. Phys.* **1998**, *12*, 620–631. [CrossRef]
41. DeBonis, J. A high-resolution capability for large-eddy simulation of jet flows. In Proceedings of the 40th Fluid Dynamics Conference and Exhibit, Chicago, IL, USA, 28 June–1 July 2010; p. 5023.
42. Bhide, K.; Siddappaji, K.; Abdallah, S. Aspect Ratio Driven Relationship between Nozzle Internal Flow and Supersonic Jet Mixing. *Aerospace* **2021**, *8*, 78.
43. Bhide, K.; Siddappaji, K.; Abdallah, S. Influence of fluid–thermal–structural interaction on boundary layer flow in rectangular supersonic nozzles. *Aerospace* **2018**, *5*, 33. [CrossRef]
44. Bhide, K. Supersonic retro propulsion: Aero-thermal-structural analysis. In Proceedings of the 7th International Conference on Jets, Wakes and Separated Flows, Tokyo, Japan, 15–17 March 2022.

45. Baier, F.; Mora, P.; Gutmark, E.; Kailasanath, K. Flow measurements from a supersonic rectangular nozzle exhausting over a flat surface. In Proceedings of the 55th AIAA Aerospace Sciences Meeting, Grapevine, TX, USA, 9–13 January 2017; p. 0932.
46. Star-CCM+ User Guide. Available online: https://support.sw.siemens.com/en-US/ (accessed on 16 July 2022).
47. Nicoud, F.; Ducros, F. Subgrid-Scale Stress Modelling Based on the Square of the Velocity Gradient Tensor. *Flow Turbul. Combust.* **1999**, *62*, 183–200. [CrossRef]
48. Cuppoletti, D.R. Supersonic Jet Noise Reduction with Novel Fluidic Injection Techniques. Ph.D. Thesis, University of Cincinnati, Cincinnati, OH, USA, 2013.
49. Heeb, N.S. Azimuthally Varying Noise Reduction Techniques Applied to Supersonic Jets. Ph.D. Thesis, University of Cincinnati, Cincinnati, OH, USA, 2015.
50. Wilson, B.M.; Smith, B.L. Uncertainty on PIV mean and fluctuating velocity due to bias and random errors. *Meas. Sci. Technol.* **2013**, *24*, 035302.
51. Lazar, E.; DeBlauw, B.; Glumac, N.; Dutton, C.; Elliott, G. A practical approach to PIV uncertainty analysis. In Proceedings of the 27th AIAA Aerodynamic Measurement Technology and Ground Testing Conference, Chicago, IL, USA, 28 June–1 July 2010; p. 4355.